



Comparative Performance of Blind Source Separation Techniques for Partial Discharge Detection in Electrical Substations

Dipak Kumar Mishra¹ · Ramesh Kumar^{2,3} · Manish Kumar Singla^{4,5} · Mohammed H. Alsharif⁶ · Zong Woo Geem⁷ 

Received: 27 September 2024 / Revised: 21 March 2025 / Accepted: 6 April 2025
© The Author(s) under exclusive licence to The Korean Institute of Electrical Engineers 2025

Abstract

The weakness or defect in electrical insulations used in High Voltage operations always leads to generation of partial discharges (PD). Partial discharges (PD) are a common by product of insulation defects in high-voltage systems. Detecting PD is a crucial aspect of power system condition monitoring. The nature of PD signals varies depending on their source, and large substations often have multiple PD sources. Ultra-high frequency (UHF) sensors offer a cost-effective and safe method for PD detection. Multiple sensors can be mounted around a substation, capturing a mixed PD signal. The Separating individual PD signals from this mix is challenging. The Techniques like the Gaussian mixture model (GMM) and Self-Organizing Feature Map (SOFM) have shown promise in this task. GMM uses time and frequency domain features, while SOFM employs continuous wavelet transform (CWT) time-frequency features. This study compares the effectiveness of these techniques for PD detection and localization using both laboratory and field experiments.

Keywords Partial discharges · Ultra high frequency · Time difference of arrival · Gaussian mixture model · Self-organizing feature map

1 Introduction

One among the basic needs for sustaining life nowadays is Electricity, therefore for a consumer uninterrupted power supply is a vital issue. It becomes a primary concern in a power transmission and distribution system to constantly monitor the equipment that are distributed over a large area. It is a tedious job when the machineries are decade old and

spread over remote locations. In maximum cases it has been found that the equipment failure is due to insulation breakdown, this issue arises from weaknesses, defects, impurities, and degradation in insulation materials. Research has indicated that structural defects and weaknesses in insulation can cause localized discharges, partially bridging the insulation between conductors. This phenomenon is referred to as partial discharge (PD) [1]. The PD starting

✉ Mohammed H. Alsharif
malsharif@sejong.ac.kr

✉ Zong Woo Geem
geem@gachon.ac.kr

Dipak Kumar Mishra
dipakmishra13@gmail.com

Ramesh Kumar
rameshkumarmeena@gmail.com

Manish Kumar Singla
msingla0509@gmail.com

¹ Department of Electronics and Telecommunication Engineering, Indira Gandhi Institute of Technology, Sarang, India

² Department of Interdisciplinary Courses in Engineering, Chitkara University Institute of Engineering and Technology, Chitkara University, Punjab, India

³ Jadara University Research Center, Jadara University, Irbid, Jordan

⁴ Department of Biosciences, Saveetha School of Engineering, Saveetha Institute of Medical and Technical Sciences, Chennai 602 105, India

⁵ Applied Science Research Center, Applied Science Private University, Amman 11931, Jordan

⁶ Department of AI Convergence Electronic Engineering, Sejong University, 209 Neungdong-ro, Gwangjin-gu, Seoul 05006, Republic of Korea

⁷ College of IT Convergence, Gachon University, Seongnam 13120, Republic of Korea

from a point with a small magnitude of electrical discharge led to complete breakage of the insulation system with successive occurrence over the time. So early detection of PD, can be a preventive measure for power supply failure [1, 2].

When partial discharge (PD) occurs within an insulator, it leads to electron breakdown avalanche of streamers, which acoustic generate waves, electromagnetic waves in the band of RF/UHF, optical frequencies, and heat energy [3]. Conventional techniques for detecting partial discharge (PD), like the IEC 60270 method, involve using a coupling capacitor to make direct contact with the test system in order to measure the short current pulses produced by PDs. Although this approach is precise, it necessitates physical contact with the high voltage terminal. Due to the limitations of this approach, various alternative techniques have been developed over the past few decades [4]. These include chemical detection methods that examine changes in the insulation's chemical configuration, high-frequency acoustic wave detection, RF/UHF electromagnetic wave detection, and optical signal detection [5, 6].

In contrast to the limitations of the acoustic method, the UHF/RF based sensor non-contact type PD system have been established that provide more practical and economical solution. The UHF band frequency signal radiated from the PD is about 100–900 MHz, which is much higher than the acoustic signal, so it can travel longer distance with lesser attenuation. Moreover, placement of the RF/UHF is safer and it imposes lesser equipment than the acoustic method, and it is possible to monitor a large power system with more accuracy. Previous studies have explored various techniques for identifying and locating multiple PD sources using multiple sensors. In one of the previous works [7, 8], the Continuous Wavelet Features (CWT) have been used for PD detection. These methods have demonstrated correlation with established standards like IEC60270 and acoustic emission analysis [8, 9].

Among the well-established techniques, ultrasonic method is most popular non-contact type method for PD detection and localization in all around the globe. This technique utilizes multiple ultrasonic sensors to detect the acoustic waves generated by the PD source within the frequency range of 30–300 kHz [4, 9]. However, it has certain limitations, such as the challenge of placing piezoelectric sensors close to high electric fields and minimizing the attenuation of high-frequency acoustic waves. Therefore, the application of this method more equipment specific and primarily designed for critical equipment of the power system, i.e., transformer.

In the RF/UHF sensor method, a suitable array antenna is located around the PD source to capture UHF signal. The antennas are placed at different locations, so that the time difference of arrival (TDOA) of signals at different locations

can be calculated and further used to find the exact PD location. Different works have emphasized on use of different antennas considering various aspects of the antenna properties like sensitivity, directivity, band width of the captured signals, gain of the antenna [10]. Also, some of the works focused on installing the antenna for complete detection of PD sources in a power system like substation, rather placing specific sensors like transformer tank [6]. The characteristic of PD signal is very much dynamic in nature, as it varies with electrode pair combination, insulation material defect used between the electrodes, voltage of operation and temperature. The propagation velocity of RF/UHF EM wave signals is very high compared to acoustic signals and very prone to surrounding noises of the same frequency range comes from multiple PD occurrence in the power system, other high frequency sources and same signal reflected by the reflecting surfaces. Also, determining accurate arrival delay times is hindered by the limitations of high-frequency digitizers. Additionally, UHF PD waveforms can follow multiple propagation paths, altering their impulsive nature. Researchers have explored various techniques, including first peak, cross-correlation, cumulative energy, and GCCPHAT, to estimate time differences of arrival (TDOA) accurately. These TDOA estimates are then used for both source detection and localization [11, 12].

Previous studies have primarily relied on time-domain characteristics of impulsive PD signals, including envelope [13], statistical properties, and time delay [11], for detection and localization. Additionally, time-power ratio maps have been used to differentiate various PD types [14]. While PD signatures exhibit variations in the frequency domain, researchers have investigated both time and frequency domain analyses for source separation. Combining time and frequency domain features offers distinct advantages over separate analyses for PD detection. The wavelet transform of any signal provides frequencies at time instances, so the time-frequency based information both separately and combinedly extracted from the nonstationary pulsating RF PD signals and can be used for PD detection. In [15] the authors have applied wavelet-based technique for de-noising of PD signal by considering automatic decomposition levels for filtering.

Since energy levels vary across different wavelet transform levels, the authors in [15] employed wavelets to cluster groups of RF PD signals. They used wavelet-based features, including skewness, kurtosis, and energy levels, to classify PD sources [16]. Researchers have proposed supervised neural network models for this classification task, requiring prior training data from the monitored substation. However, obtaining adequate training data for new substations can be challenging. To address this, blind source separation algorithms have been implemented to separate mixed

time-domain signals received by sensors, facilitating signal identification [17]. Due to the limitations of the supervised learning, the unsupervised techniques are proved to be more efficient. In [7] Gaussian Mixture Model (GMM) based unsupervised technique and in [8] Self Organized Feature Map (SOFM) based unsupervised classification techniques have been applied on different PD extracted features. These features are from both time and frequency domain-based features and the results have been obtained are very much satisfactory. As, both the techniques have been tested on laboratory and field-based experiments, so more comparative study between the two established techniques is needed. It may help us to establish one suitable solution in finding an efficient PD classification technique and further may help us for customize the error in PD detection and localization. In the present study the efficiency of two unsupervised techniques is compared for classification of the PD sources.

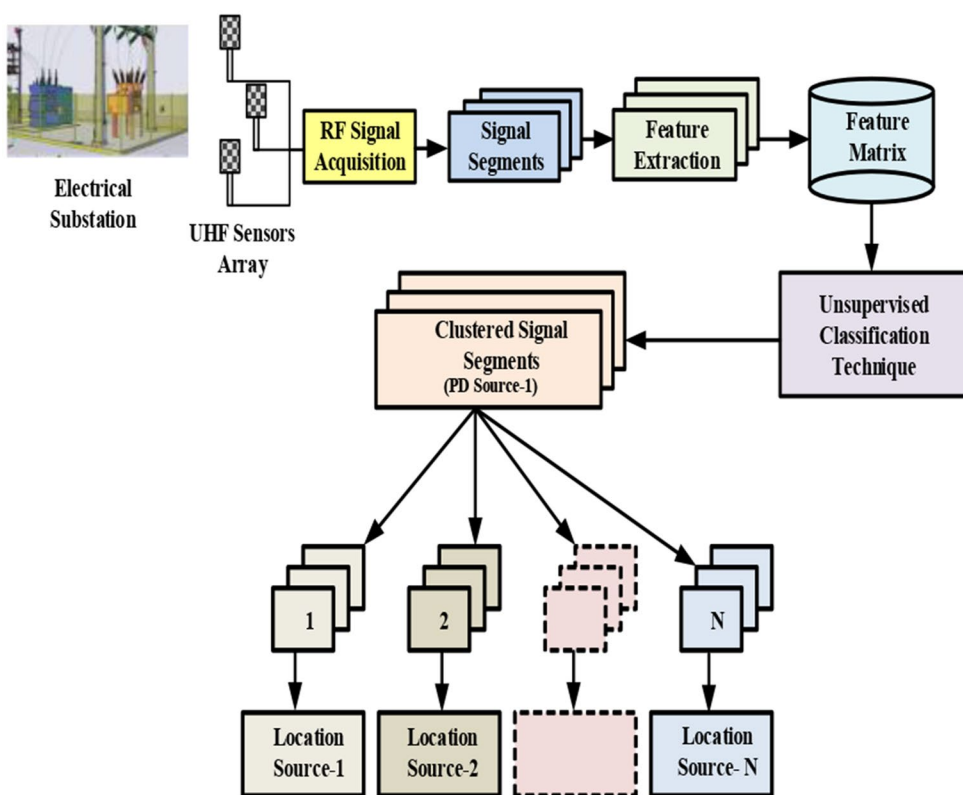
This study presents a method for automatically detecting and localizing individual PD sources within the power system, as shown in Fig. 1. Impulse waveforms of PD were collected from field-based UHF antenna sensors over extended periods. These waveforms were pre-processed for feature extraction. While multiple reflections from various surfaces can alter the impulse waveform shape, the fundamental frequency domain features of a specific PD source remain relatively invariant. After pre-processing of the signal, the wavelet transform of the signal segments are taken and further wavelet-based signal features are extracted from

them. These features collected from a particular sensor then arranged to form a feature matrix which is further used by the classifier technique to find the PD signal source. Considering different situations and data parameters, many feature matrices have been made for testing. For finding the efficient classifier, the two well established unsupervised classification techniques have been tested, i.e., Gaussian Mixture Model (GMM) and the self-organizing feature map (SOFM) through ML algorithm based model. To estimate time-delay-of-arrival (TDOA) for source localization, a subset of the best-classified signal segments, along with their corresponding waveforms from the other three sensors, were used. For improved accuracy, the average of the locations from this subset was calculated.

2 Materials and Testing Procedure

This study investigates the characteristics of PD-related signatures in radiated UHF signals, including variations across different PD sources and noise. To facilitate these investigations, we developed an array of microstrip patch antennas with a bandwidth of 200–800 MHz and a center frequency of 500 MHz with signal conditioning and amplification circuitry are associated. The following sections detail the sensors of UHF, signal acquisition, and both laboratory and field-based testing procedures.

Fig. 1 Flow diagram of the proposed scheme



2.1 Signal Conditioning with Sensor Module

Micro-strip patch antennas, meeting the specified requirements, were strategically placed around the PD source area to capture radiated RF signals within the RF/UHF frequency band. The micro-strip antenna's robust construction, ease of manufacturing, lightweight design, and adaptability to specific frequency bands made it an ideal choice. The captured antenna signals, characterized by low magnitudes (tens of micro-Volts) and wideband noise, required an amplification and signal conditioning with high-gain amplifiers and filters. Figure 2 illustrates the functional block diagram of the detection system. Impedance matching circuits were included for proper signal conditioning, while a constant DC power supply unit, comprising a step-down transformer and bridge rectifier, provided power to the signal conditioning unit. Shielding was employed to isolate the power supply and conditioning units from external interference, preventing power line coupling and other unwanted influences. A signal detection sensor and signal conditioning unit were set up to work between 200 and 800 MHz, with a middle frequency of 500 MHz. This range was good for our experiment. The processed signal was sent to a digital storage oscilloscope to see and save as parts of the signal.

For handling the challenges of voltage stress the EM wave sensing system often include improved EMI suppression techniques, such as snubber circuits, shielded inductors, and optimized PCB layouts to reduce parasitic inductance and capacitance. Moreover, soft-switching techniques or resonant converters can reduce high-frequency switching noise. For better thermal management strategies, more efficient heat sinks, advanced packaging, or using materials with higher thermal conductivity are used. The advantages of using a soft-switched resonant tank in this topology is to minimize electromagnetic interference (EMI) reduction, minimize the switching losses associated with transistor, for better thermal management, improving efficiency and

for better high frequency operations and for control and regulation.

2.2 Testing in Laboratory

Lab tests were performed with various artificial PD sources. These sources involved a pair of closely spaced electrodes, one charged and the other grounded, with an insulating substance between them. To analyse the impact of insulating material, electrode type, and electrode gap on radiated UHF signals, extensive experiments were performed. Different electrode combinations, including sphere-sphere, needle-flat, and flat-flat, were tested with various insulating materials (oil, air, solid) and gap lengths. Solid insulators included acrylic discs, kraft paper, and oil-impregnated paper, while transformer oil and natural air were used as liquid and gas dielectrics, respectively. Tests were also done using solid insulation with varying void sizes. Figure 3a and b illustrate the lab experiment and its functional block diagram.

For artificial PD source excitation, PD sources i.e., one of 300 kV and other two of 100 kV (as shown in Fig. 3), have been used. Four identical UHF signal sensing units, each equipped with a micro-strip patch antenna, filter, and amplifier, were strategically positioned to capture radiated RF impulsive waveforms from single or multiple sources. The amplified signals were sent to a high-speed digitizer with a maximum sampling rate of 5 giga samples per second. All connections were made using identical, noise-shielded cables of the same length.

Laboratory experiments were conducted using both single and multiple PD sources of varying types. To understand the influence of reflecting surfaces, applied voltages, and source-sensor distance on radiated PD patterns, tests were performed with and without reflecting surfaces present. Additionally, other impulsive signals generated by switching operations in high-voltage transformers, fluorescent lamps, tap changers, IGBT-based motor drives, relays, Wi-Fi, and mobile devices were captured by the sensors.

Fig. 2 Functional block diagram of the RF sensing unit with microstrip patch Antenna

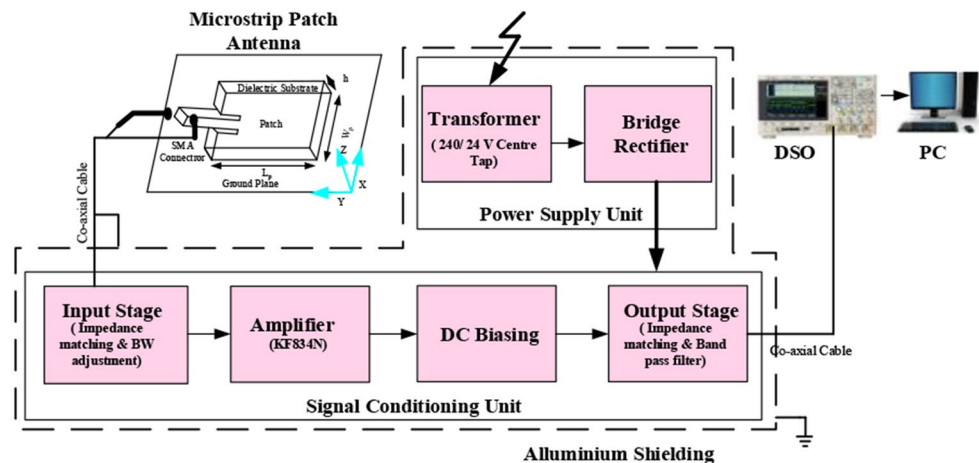


Fig. 3 (a) Functional block diagram of laboratory-based testing facility. (b) Photograph of actual laboratory testing

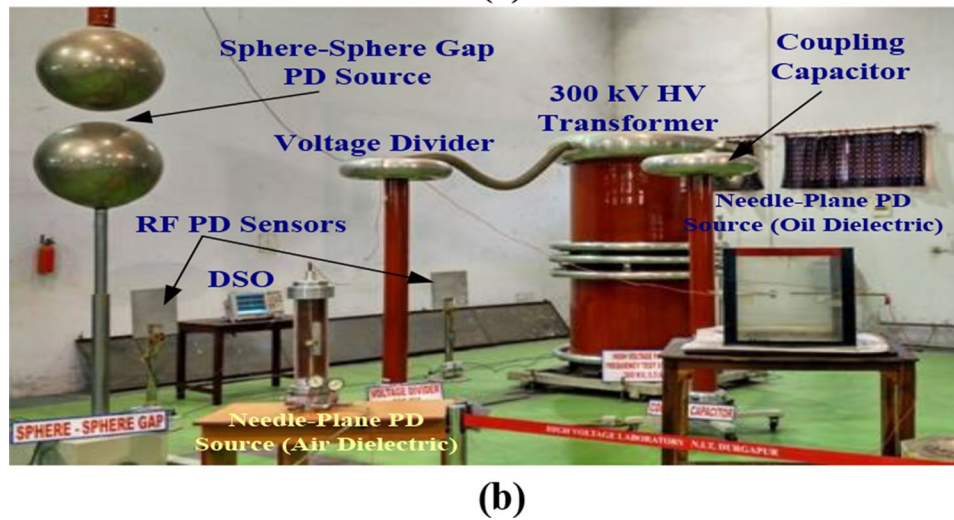
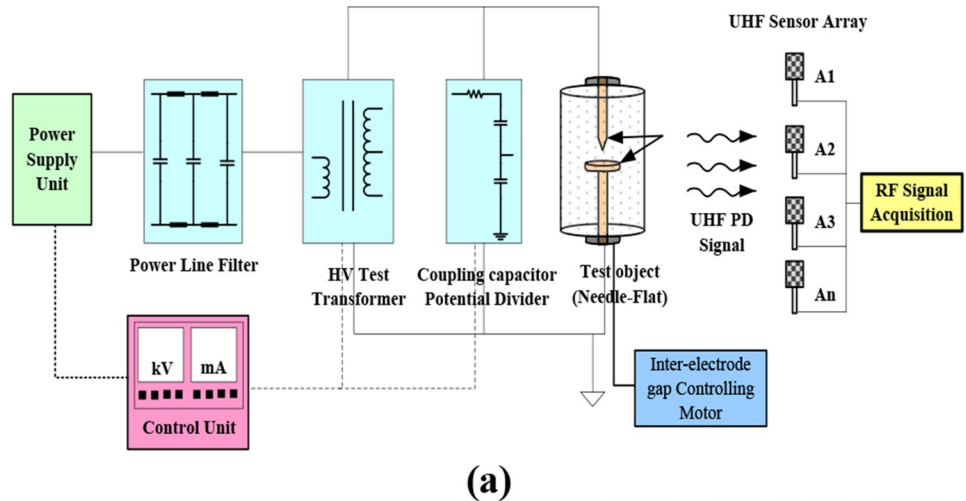


Table 1 The types PD sources for lab tests

S. No.	Medium with Gap/Void	Type of electrode		
		Needle-Flat	Flat-Flat	Sphere-Sphere
1	Air (Gap in cm)	1, 3, and 4	1, 3, and 4	5, 20 and 30
2	Oil (Gap in cm)	0.5, 1, and 2	0.5, 1, and 2	1, 2, and 3
3	Solid (Dia in cm)	0.05, 0.1, and 0.3	0.05, 0.1, and 0.4	0.1, 0.3, and 0.5

Testing was conducted in phases. Initial tests involved single PD sources in open space, followed by tests with obstacles present. To analyze directivity and attenuation characteristics, antenna positioning was varied. In subsequent phases, multiple PD sources were tested in various combinations, including air-air, oil-solid, and air-solid. All laboratory test results, captured as raw time-domain signals, were recorded for analysis.

2.3 Testing on Field

To validate the proposed PD detection and localization method in real-time conditions, field testing was conducted at three different distribution substations. Table 1 provides details of these substations, while Fig. 4 shows a photograph of testing location with the RF sensing unit, Table 2 provides the detail of the field-testing details of substations.

2.4 Pre-processing of the Signal

Following the successful data recordings by the sensing unit from the various types of PD sources, the background noises have been eliminated and PD impulses identified with an developed automated system. Raw signals were initially filtered using a 10-point moving average filter. The apparent starting point of each impulse was determined by identifying the maximum value of the signal’s derivative. The end point was considered when the average signal strength dropped to 30% of the peak value. A Hamming window function was

Fig. 4 Photograph of field testing

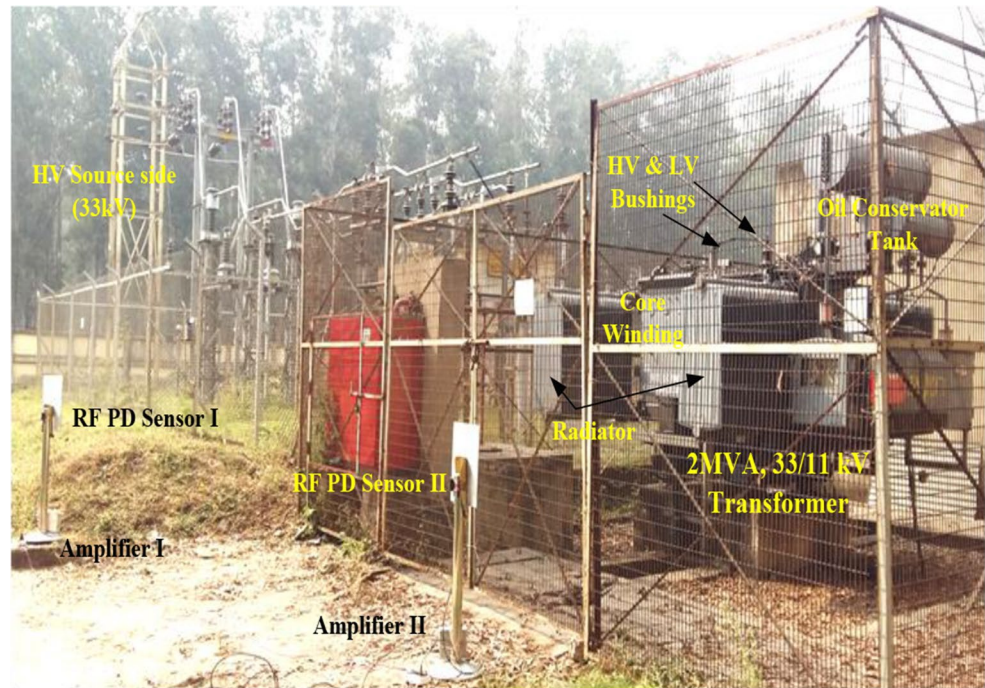


Table 2 The field-testing details of substations

Parameters	Substations		
	1	2	3
Voltage ratings	33/11 kV	33/11 kV	33/11 kV
Dimensions (m ²)	157 × 121	89 × 121	44.5 × 121
Transformer ratings	2 MVA x 2	1 MVA x 2	2 MVA x 1

used to remove background noise from the unfiltered raw signal. The window length was proportional to the duration of the impulse in the signal segment.

3 Methodology of Detection for PD Source

This section outlines the procedures for PD source detection and localization using recorded signal segments from laboratory and field testing. Different signal characteristics, such as time, frequency, and time-frequency features, were calculated from the raw signal, its spectral density, and the continuous wavelet transform (CWT) signals. Then the feature matrices formed by the signal features tested by different unsupervised learning techniques like GMM and SOFM for establishing an analysis for efficient blind source PD detection.

3.1 Feature Extraction

Once background noise was removed from the raw time-domain signals, a thorough analysis was performed to examine the time-domain and frequency-domain characteristics of the partial discharge waveforms. Time-domain

parameters, including peak value, impulse duration, and front and tail times, were extracted using appropriate signal processing techniques. Time-delay-of-arrival (TDOA) measurements between different RF sensors are crucial for source localization. Following previous research [11], the first peak method was found to be more accurate for TDOA estimation.

3.1.1 Time Domain Based Features

The shape and characteristics of the impulsive PD waveforms were analysed by examining the absolute values of the recorded time series data. These features, which describe the waveform in the time domain, include the peak value (the highest point), the front time (the time from the start to the peak), the tail time (the time from the peak to 30% of the peak), and the pulse duration (the length of time the waveform remains above 50% of its peak).

3.1.2 Frequency Domain Based Features

To analyze the signal in the frequency domain, we calculated the Power Spectral Density (PSD) of the pre-processed time series data. For this, the data was divided into overlapping segments of length M , and each segment was multiplied by a window function $w(n)$. Period grams were computed for each windowed segment, and their average was then calculated. For a segment of signal $x(n)$, $\{x_i(n)\}$ are data segments where $i=1,2,\dots$ $i = 1, 2, \dots S$. The Welch spectrum estimate [18] is given by (1) and (2),

$$\hat{P}_w(f) = \frac{1}{S} \sum_{i=1}^S \hat{p}_i(f) \tag{1}$$

$$\hat{p}_i(f) = \frac{1}{M} \frac{1}{P} \left| \sum_{n=1}^M w(n) x_i(n) \exp(-j2\pi fn) \right|^2 \tag{2}$$

Where $\hat{p}_i(f)$ is the periodogram estimate of i th segment, $w(n)$ is data-window, M is window sequence. P is given as $P = \frac{1}{M} \sum_{n=1}^M |w(n)|^2$ P represents the normalization for the power in the window function. $\hat{P}_w(f)$ is PSD.

The frequency with the highest power is called the peak power frequency (PPF) and represents the main frequency of the radiated RF PD signal. The median frequency (MF) is the point where half of the signal’s power is above and half is below. The bandwidth, measured using the full-width-at-half-maximum (FWHM), shows if there are multiple frequency components present. Spectral entropy (SE) quantifies the disorder or flatness of the PSD, calculated using Shannon’s entropy $SE = -\sum_i P_i \ln(P_i)$ where P_i is the normalized value of the PSD at each spectral component with a bandwidth of one spectral unit.

3.1.3 Continuous Wavelet Transform (CWT) Based Features

The CWT features were extracted from the pre-processed PD signal segments. Unlike individual time and frequency domain analyses, CWT offers the advantage of providing two-dimensional time-frequency information. The multi-resolution analysis capability of CWT allows for time windows for high frequencies and long-time windows for low frequencies, enhancing both time and frequency resolution. As the name implies, a wavelet ‘ ψ ’ can be described as a small wave that has a limited duration and its amplitude oscillates equally on both sides of the axes with a mean value of zero, i.e., $\int_{-\infty}^{+\infty} \psi(t) dt = 0$. For a given time domain signal $x(t)$ with scale parameter ‘ s ’ and translation parameter ‘ τ ’, the CWT can be represented as

$$W(s, t) = \frac{1}{\sqrt{s}} \int_{-\infty}^{+\infty} x(t) \psi\left(\frac{t-\tau}{s}\right) dt \tag{3}$$

ere, $W(s, t)$ is the CWT coefficient representing the correlation between the time series signal section under consideration and the scaled and time-shifted version of the mother wavelet. The greater the value of the coefficient $W(s, t)$ more is the similarity between them. CWT calculates the coefficients at every possible scale and time instant. The time series signal can again be recovered from $W(s, t)$ by

inverse continuous wavelet transform (ICWT). The choice of mother wavelet significantly impacts the wavelet pattern. Selecting an appropriate mother wavelet and its corresponding algorithm is crucial for optimal results. In this study, the Gaussian wavelet was found to be suitable and was therefore used in the proposed model.

Several features were extracted from the continuous wavelet transform (CWT) coefficients of the signal segments. These included the CWT peak (defined by its scale, position, and strength), the time differences between consecutive peaks and the highest peak, the energy of the frequency band associated with the highest peak, and the bandwidth (the range of dominant frequencies at the CWT peak, determined using FWHM). These features were found to be suitable for the proposed model. The Sub-band scale entropy, a measure of disorder or uncertainty, was found to be a suitable feature for PD classification in conjunction with bandwidth [19]. The entropy was calculated for the scale corresponding to the CWT peak and along the translation axis. The entropy of the scale set S_i is then defined as:

$$H_i = -\sum_{j=1}^m p(x_{ij}) \log_{ap}(x_{ij}) \tag{4}$$

This case, the base of the logarithm (a) is usually set to 2, which means the entropy is measured in ‘bits.’ Sub-band scale entropy measures how much the time series fluctuates at the scale of the highest peak. A lower entropy value means there are more random fluctuations, while a higher value indicates more regular patterns in the time series.

3.1.4 Feature Matrix

All the extracted features, including time-domain, frequency-domain, and CWT characteristics, were arranged in a matrix. Each row of this matrix represents the features of a specific signal segment. These rows are called feature vectors, and the matrix containing feature vectors from a particular PD source type is called a feature matrix [20]. For each type of artificial PD source, three feature matrices were created based on recordings with small, medium, and large gaps or voids (as shown in Table 1). These feature matrices represent a specific PD source with a fixed gap, insulation, electrode type, and sensor-source distance, but with varying applied voltages within a suitable range. Table 3 shows an example feature matrix with normalized feature values. Another group of feature matrices was created using recordings from artificial PD sources tested near reflecting surfaces and obstacles. Two more groups of feature matrices were formed using lab tests with multiple PD sources, both with and without reflecting surfaces. These

Table 3 Example of feature matrix

Feature vector number	Features				
	Tail time	Peak value	Front time	Spectral entropy	Bandwidth
1	0.45	0.75	0.34	0.39	0.71
2	0.45	0.79	0.33	0.41	0.72
3	0.46	0.74	0.33	0.41	0.67
:	:	:	:	:	:
N	0.48	0.78	0.35	0.38	0.70

experiments included various combinations of artificial PD sources, starting from two and increasing to ten simultaneously active sources. The presence of multiple PD sources was identified using an unsupervised method called Greedy GMM, which is briefly explained below (see [21] for more details).

3.2 Gaussian Mixture Model (GMM)

A Gaussian mixture density is a weighted sum of mixture component densities. Let \vec{x} be a d-dimensional feature vector, $\vec{x} \in R^d$. The Gaussian mixture density can be described as,

$$p(\vec{x}|\theta) = \sum_{k=1}^M \omega_k p_k(\vec{x}) \tag{5}$$

where, M is the no of mixture components and ω_k $k = 1, \dots, M$ are the mixing parameters. $p_k(\vec{x})$, for $k = 1, \dots, M$ are the individual component densities. The individual component densities are given by Gaussian distribution functions of the form,

$$p_k(\vec{x}) \sim \mathcal{N}(\mu_k, S_k) = \frac{1}{(2\pi)^{\frac{d}{2}} |S_k|^{\frac{1}{2}}} \exp \left\{ -\frac{1}{2} (\vec{x} - \mu_k)^T S_k^{-1} (\vec{x} - \mu_k) \right\} \tag{6}$$

where, mean μ_k is a d-dimensional vector and S_k is a $d \times d$ covariance matrix, and $|S_k|$ is the determinant of S_k . The complete Gaussian mixture density is parameters are represented by θ where $\theta = \{\omega_k, \mu_k, S_k\}; k = 1, \dots, M$. The objective is to determine the number of Gaussian mixture components (K) and their parameters (μ_k, Σ_k, π_k) for a given feature matrix. The EM algorithm is commonly used to estimate these parameters [21]. Recently, Greedy learning of GMM has been proposed, which inherently estimates the model order through an iterative process. This approach maximizes the likelihood of the parameters for the given data set.

This estimation aims to identify the optimal parameter values by maximizing the likelihood function derived from the feature matrix. Let $X = \{\vec{x}_1, \vec{x}_2, \dots, \vec{x}_N\}$ represent a set of NNN vectors independently sampled from a single

distribution characterized by the probability density function $p(\vec{x}|\theta)$. The joint probability density of the entire data-set can be expressed as $p(X|\theta) = \prod_{n=1}^N p(\vec{x}_n|\theta) \equiv L(\theta)$

where $\mathcal{L}(\theta)$ denotes the likelihood function for θ given X. The maximum likelihood (ML) estimation seeks to determine θ that maximizes this likelihood function.

$$\hat{\theta}_{ML} = \arg \max_{\theta} L(\theta) = \arg \max_{\theta} \prod_{n=1}^N p(\vec{x}_n|\theta) \tag{7}$$

In order to be maximum, $\hat{\theta}_{ML}$ must satisfy the necessary condition that is, the gradient of the likelihood function with respect to θ be zero.

$$L(\theta) = \ln L(\theta) = \ln \prod_{n=1}^N p(\vec{x}_n|\theta) = \sum_{n=1}^N \ln \{p(\vec{x}_n|\theta)\} = \sum_{n=1}^N \ln \left\{ \sum_{k=1}^M \omega_k p_k(\vec{x}_n) \right\} \tag{8}$$

An iterative approach is crucial for locating the global maximum of $\ln [p(X|\theta)]$ since the optimal $\hat{\theta}_{ML}$ cannot be determined analytically for mixture models. The Greedy GMM method begins with a single component M=1, and progressively adds one component at a time to the mixture.

There are many ways to model uncertainty, each suited to different types of problems and systems. Bayesian Inference is a framework that allows us to update our beliefs about the world as new data comes in. The uncertainty is represented by probability distributions over parameters or hypotheses [22–25].

Self Organized Feature Map (SOFM) Based Classification The Self-Organizing Feature Map (SOFM), a machine learning algorithm based on neural networks, is often called Kohonen’s net. This classifier mapping model consists of four main steps: initialization, competition, cooperation, and adaptation. In an n-dimensional input vector space, each node i is considered a Kohonen’s input neuron, connected to other neurons in a rectangular or hexagonal arrangement. The winning Kohonen’s neuron k is the one with the smallest Euclidean distance.

$$D = \|x - \omega_k\| = \min_i \{ \|x - \omega_i\| \} \tag{9}$$

The weight vectors of the winning neuron and its neighboring neurons, the learning rate function $\eta(t)$, drawing them closer to the input vector. The learning rate function $\eta(t)$ ranges from 0 to 1. This iterative updating process continues until a stable mapping is achieved.

$$\omega_i(t+1) = \omega_i(t) + \eta(t) [x - \omega_i(t)] \tag{10}$$

4 Results

4.1 PD Characterization

Different tests have been conducted to know the characteristics of the RF PD signal at different conditions like electrode pairs, the variation of the gap between the source and the sensors, and with presence and absence of reflecting surfaces around the sensing unit. Before considering the signal features as discussed in the last unit, the feature variation with different conditions should be studied. So, at different above-mentioned conditions, the time, frequency, and CWT

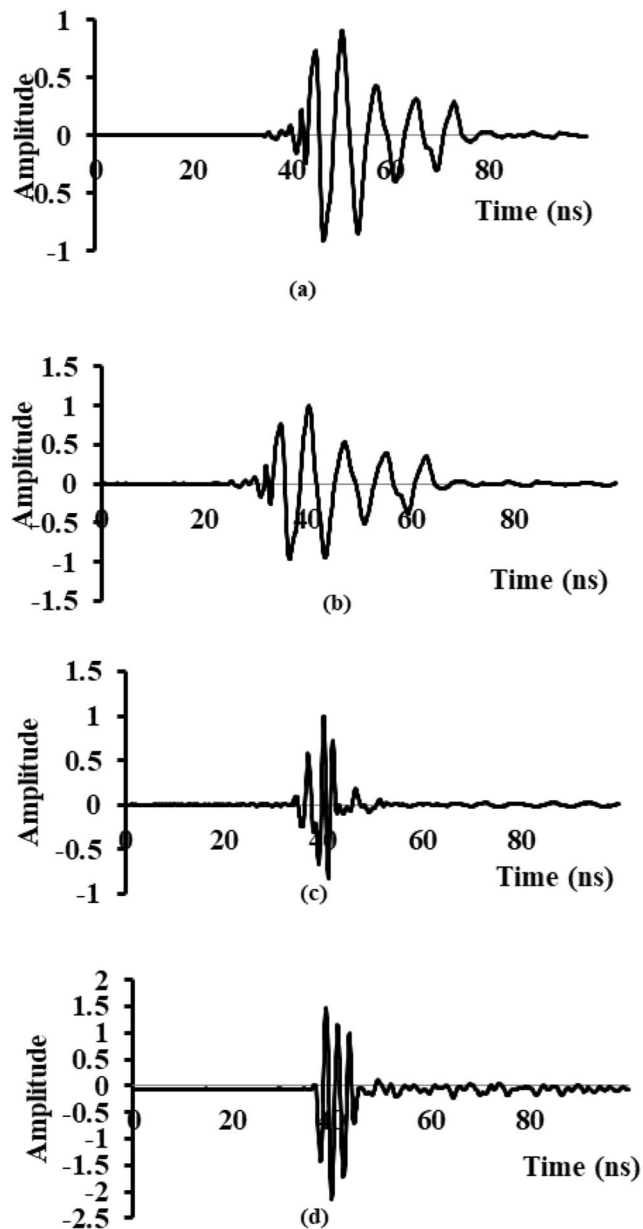


Fig. 5 Flat-needle electrode of PD signal with, (a), (b) Air insulator captured by antennas of same PD, (c) Oil and (d) Solid insulation

features have been studied. In the initial phase of the study, a single artificial partial discharge (PD) source was activated in a controlled laboratory setting. Each source had a unique electrode pair configuration. An array of four antennas was positioned around the source to ensure a direct path for the emitted ultra-high-frequency (UHF) signal. This experiment was repeated multiple times using different PD sources and varying test conditions.

Analysis of the recorded signals reveals their impulsive and dynamic characteristics, along with the presence of continuous background noise. Figure 5 illustrates sample PD signals captured using a Needle-Flat electrode pair and various dielectric mediums. Figure 5a and b show the impulsive radio frequency (RF) waveforms emitted by a typical PD source with air insulation. These waveforms were recorded by two antennas placed at different distances from the source. While the impulsive nature of the waveforms remains largely consistent, a significant time delay is observed between them. This is attributed to the closer proximity of the antenna that captured the signal in Fig. 5 compared to the one in Fig. 5. Figure 5c and d present signal segments from the same Needle-Flat electrode pair but with different dielectric media: liquid (transformer oil) and solid (acrylic disc). Comparing Fig. 5a, c, and d, it becomes evident that the characteristics of the impulsive waveforms change significantly as the nature of the PD source varies. The shape nature of the impulses and frequency of oscillations is changing quite significantly. A similar type of study can also be done with the CWT features. The CWT representations shown in Fig. 8a, b, and c are of the PD sources of different dielectric mediums, i.e., air, liquid, and solid. The nature of these figures is quite different. Figure 8c and d represent PD sources with solid dielectric insulation and with the same electrode configuration but with different inter-electrode gaps.

To understand the frequency nature of the signal, the PSD of the time domain signal has been found. The Scaled PSD coefficients of different PD sources with different insulations are shown in Fig. 7a. In this figure, there are three different groups of signals formed by three different dielectrics, i.e., solid, liquid, and air. It has been observed that the frequency nature of a specific dielectric remains the same with variations in inter-electrode gap and distance between the PD source and antennas.

The PD signal segment as shown in Fig. 6 is the PD source with solid insulation but at a different inter-electrode gap other than represented in Fig. 5(d). The number of oscillations in both waveforms is nearly identical. Figure 6 shows the same PD source captured with a reflecting surface obstructing the propagation path emitted UHF signal. A detailed analysis shows that the time-domain characteristics are affected not only by changes in the PD source but

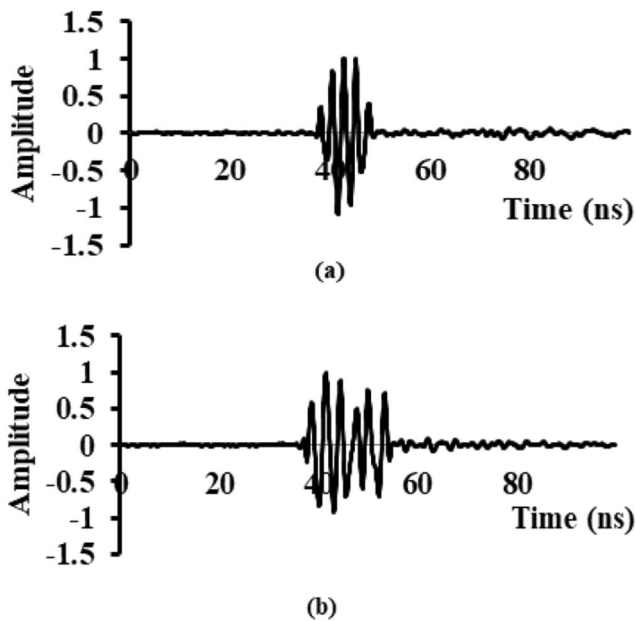


Fig. 6 The flat-needle electrode of PD signal with solid insulation (a) electrode gap (b) multiple reflections

also by the presence of obstacles or reflecting surfaces in the signal's path. However, comparing the frequency-domain characteristics of a PD source with and without a reflecting surface, as shown in Fig. 7b, suggests that reflecting surfaces or obstacles have little impact on these characteristics.

Wavelets are effective for analysing signals in both time and frequency domains, so we applied the CWT to all recorded waveforms from various experiments. Figure 8a, b, c, and d display the surface plots of the CWT (magnitude) coefficients derived from the signal segments shown in Fig. 5a, c, d, and 6(a), respectively. These surface plots represent the magnitude of the CWT coefficients on the vertical axis, while the other two axes indicate scale and translation/position (sample number). By examining these plots, we can observe that the peaks correspond to the peak points of the oscillatory impulsive signals, and the associated scale values reveal the frequencies of these peaks. The wavelet transform provides a detailed view of the frequency components present at each time instant. Furthermore, Fig. 8a, b, c and d more clearly illustrate variations in frequency-domain characteristics throughout the impulsive UHF signal. However, the transformation from a one-dimensional time series signal to a two-dimensional representation result in a significant increase in data points (due to the number of scales). This can pose challenges for subsequent processing tasks, such as PD source detection. To address this, five key CWT features were extracted in this study, as detailed in Sect. 3.1.

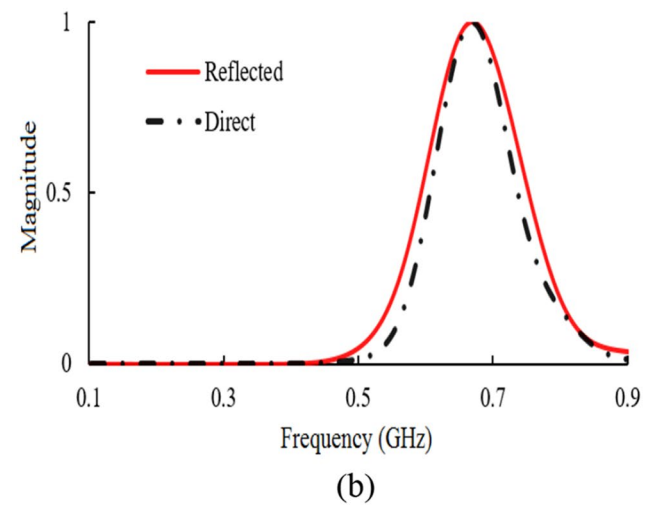
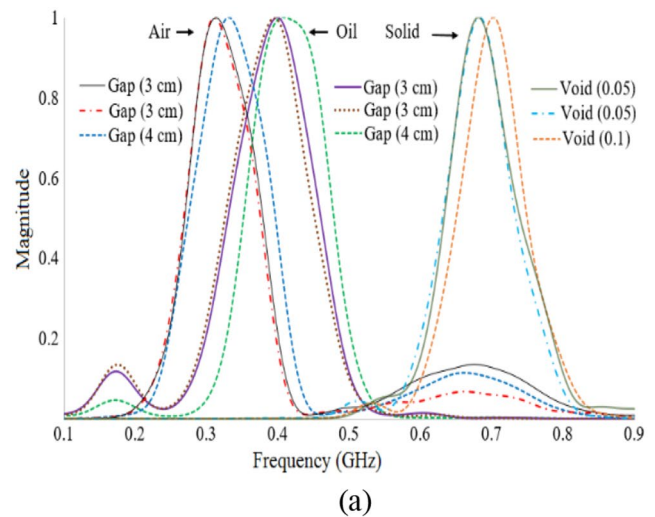


Fig. 7 (a) PD sources of PSD coefficients (b) Direct and reflected signal-based SD coefficients

4.2 Detection of PD Sources

After the acknowledgment of the PD behaviour with the changing conditions, it is necessary to identify the PD source from the detected behavioural characteristics. As PD nature is highly stochastic, the application of unsupervised classification techniques will have a special advantage over the supervised learning technique. In this study two unsupervised techniques as mentioned before have been implemented for successful PD source detection, i.e., GMM and SOFM techniques, and the results are compared. These techniques have been tested upon the input feature matrices formed from the PD characteristics described as follows.

As previously noted, features from various domains such as time, frequency, and continuous wavelet transform (CWT) were combined to form a Feature Matrix for multiple PD sources. These features were categorized into two groups: position or time-based features (P/T) and scale

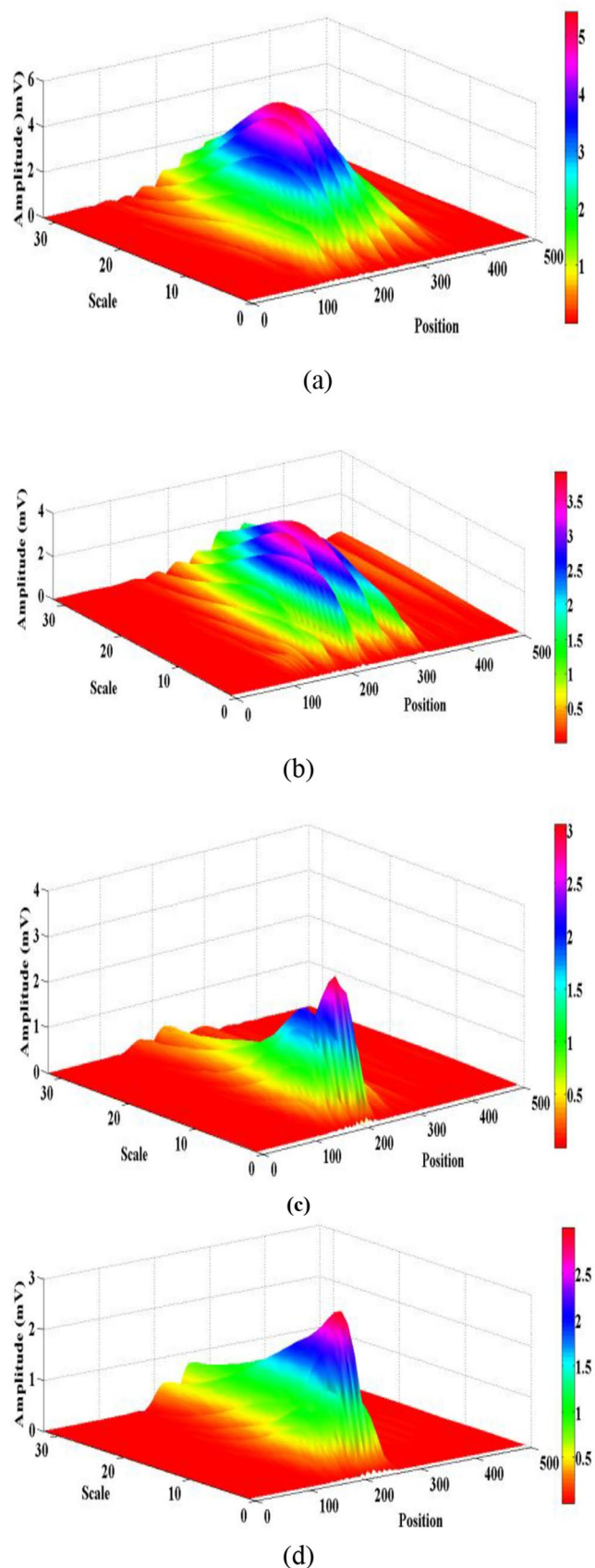


Fig. 8 CWT of PD signal, with (a) Air, (b) Oil, (c) Solid and (d) Solid with different inter electrode gap condition

or frequency-based features (S/F). Time-domain features include the CWT peak, peak-to-peak duration, and all other time-domain measurements. In contrast, frequency-domain or scale features encompass CWT sub-band scale energy, bandwidth, sub-band scale entropy, and all power spectral density (PSD) features. Figure 9 illustrates how three distinct features pulse duration, front time, and bandwidth vary across five different PD sources with various insulation types. Despite some variations, features from different sources generally form distinct clusters, suggesting that they can be differentiated. Notably, some PD sources exhibit significantly higher variance than others, reflecting differences in the time and frequency-domain behaviour of specific PD sources across successive events.

4.2.1 PD Detection Through GMM

To assess the GMM model, a variable mixed feature matrix was first generated by randomly combining feature matrices from individual PD sources tested in free space. The number of combinations (C) was adjusted by varying electrode type, insulation, and electrode gap/void size. Although theoretically, up to 3240 combinations are possible with two PD sources, the study was confined to 250 random combinations (for $C=1$, up sampling was used). The mixed feature matrix was then analyzed with the GMM to determine the optimal number of model components (M best) that minimized either the Bayesian Information Criterion (BIC) or the Akaike Information Criterion (AIC). Accurate identification occurs when M matches C . Table 4 provides a summary of the GMM's average performance in correctly identifying the number of PD sources across multiple runs for different datasets. The leftmost column indicates the actual number of PD sources in the mixed feature matrix, while the other columns display the percentage of times the GMM accurately identified this number in 250 cases under various conditions, including the number of feature vectors (N) per PD source. With $N=30$, the average performance across all 10 cases was 97.5%, reflecting strong accuracy. However, performance declined with fewer sources, particularly for a single PD source ($C=1$). Additionally, reducing the number of examples (N) to 10 led to a notable decrease in performance, down to 93.0%.

Further analysis revealed that the GMM overestimated the number of PD sources when the number of sources was low and when the number of examples (N) was insufficient. This was attributed to convergence issues with low variance during optimization. To maximize the likelihood, the GMM might have mistakenly assigned one or two examples to a new, incorrect category. To address this, a variance-limiting constraint was introduced during the EM algorithm estimation. The experimentally determined optimal value of 0.04

Fig. 9 Scatter plot of pulse duration vs. front time vs. bandwidth for five different PD sources

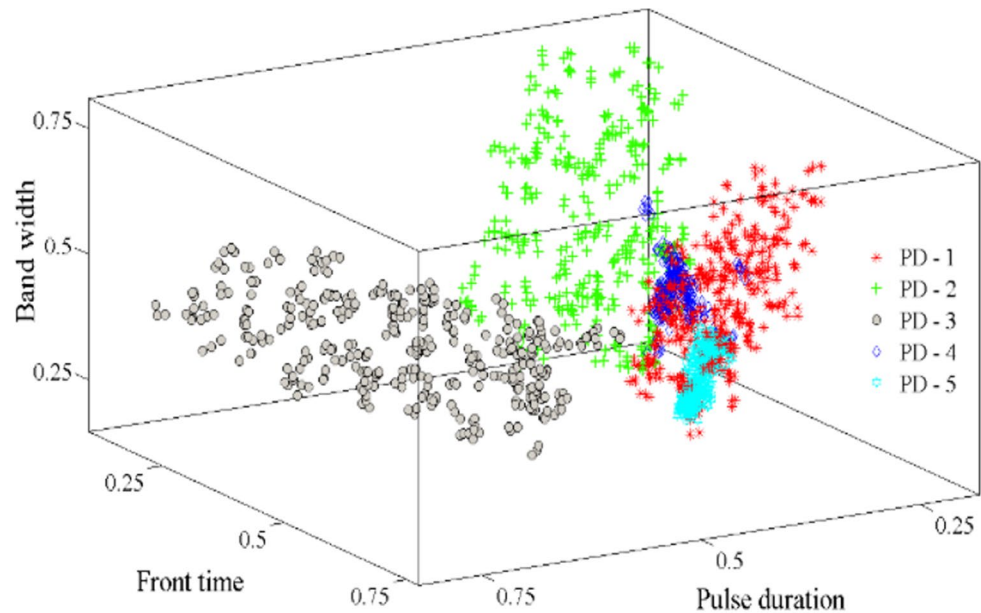


Table 4 Performance PD sources (detection) through GMM model

No. of PD	Variance > 0		Variance > 0.04					In presence of obstacle	
	Free space		Free space			N=4	3 ≤ N ≤ 30	N=15	3 ≤ N ≤ 30
	N=30	N=10	N=30	All					
			P/T	S/F	All				
1	87.9	74.6	85.1	97.3	96.8	98.2	98.3	97.2	97.4
2	94.6	84.3	89	100	99.2	99	98.9	100	99.7
3	98.8	92.7	93.3	99.9	100	100	100	100	100
4	100	97.1	95.9	98	99.5	99.7	99.5	98	100
5	99.6	98	98.2	100	99.7	99.8	98.8	100	99.1
6	98.5	97.6	91.7	99.7	99.7	100	100	99.5	100
7	99.7	94.8	92.6	99.2	100	99.1	97	100	96.8
8	100	96.5	94.4	97.5	100	99.8	98.4	97.5	95.9
9	99.3	100	91.9	99.6	100	96	97.5	100	94.4
10	97	94	92	96.5	100	93.9	95.3	96.5	92.5
Average	97.5	93	92.4	98.8	99.5	98.6	98.4	98.9	97.6

resulted in improved overall performance, especially for low numbers of sources. However, with N reduced to 4 from 30, performance degraded, particularly for higher numbers of sources (9 and 10). This is likely due to the insufficient number of examples, leading the GMM to fail to identify separate classes.

The different tests were conducted with considering only position or time domain features (P/T) in the feature matrix then with only scale or frequency domain features (S/F) and finally considering all features. This result with $N=30$ has been presented in Table 4. Analysis indicates that time-domain features alone achieve an accuracy of 92.4%, while frequency-domain features reach 98.4%. Combining both features further enhances accuracy to 99.5%. The GMM was similarly evaluated using feature matrices obtained from PD source testing in the presence of reflecting surfaces and obstacles. While performance decreased slightly, it

wasn't significantly impacted by obstacles. The minor drop in performance might be attributed to the increased complexity of reflected impulsive waveforms

4.2.2 PD Detection Through SOFM

A feature matrix combining three different PD sources with varying insulation media was initially tested using the SOFM model. Each source, consisting of 50 PD signal features, created a 150×5 matrix that was input into the testing model. The neural network was trained with a 12×12 dimension size. Figure 10 shows the neural output SOFM neighbor distance plot, where neurons are represented by hexagons and inter-neural distances by colour codes. In Fig. 10, the three clusters represent the three PD sources.

To examine the contribution of different features in the input feature vector for PD source clustering, tests were

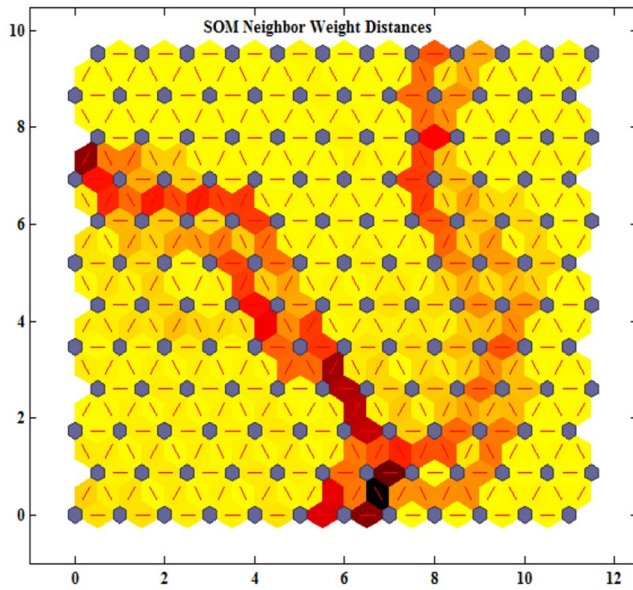


Fig. 10 12 × 12 neighbor weight distance SOFM plot

conducted in open space and with reflecting surfaces or obstacles. Initially, tests were performed with two feature categories separately, followed by a combined analysis. When only position features were considered, accuracy in PD determination significantly decreased in the presence of reflecting surfaces compared to open space. However, scale features showed less variation. Combining all features significantly improved accuracy. These results indicate that time-domain signals are more susceptible to multiple reflections than frequency-domain signals.

Additionally, increasing the number of features (N) enhances clustering and accuracy. Different feature matrices were tested with varying numbers of ‘N’ for the same PD source. As ‘N’ increases, the clusters become more prominent with darker and thinner boundaries. The study

also examined inter-class and intra-class PD source signals. Inter-class PD sources have different dielectric materials, while intra-class PD sources have the same dielectric material but vary in the distance between electrodes/void size and the combinations of electrode pairs. Different feature matrices were analyzed individually and collectively for separate classes of PDs. There are 351 possible intra-class PD source combinations and 3240 total combinations. For this test, 100 intra-class and 100 inter-class combinations were created with varying numbers of PD sources (ranging from 1 to 10).

Observations indicate that for intra-class feature matrices, time or position features are more crucial for clustering accuracy than scale features. Conversely, in inter-class tests, both types of features contribute equally to accuracy. In inter-class scenarios, increasing ‘N’ for each PD source generally enhances accuracy, particularly with a larger number of sources. Tests involving PD sources with obstacles suggest that reducing ‘N’ might lower accuracy, likely due to the increased complexity and less variability in the feature vector. A summary of these findings is presented in Table 5.

4.3 Localization of PD Sources

Once the accurate number of PD sources is determined, the next step is to locate their positions. The localization method, using four sensors, involves solving nonlinear equations using the Newton-Raphson method as described in [11]. Tables 6 and 7 show how well the GMM and SOFM techniques localized PD sources in lab and field tests. We placed PD sources at various distances from four antennas and calculated the localization error as the ratio of the distance between the estimated and actual locations to the average distance between the source and the antennas. S1–S4 represents the distances to antennas 1–4.

Table 5 Performance evaluation of number of input feature vectors

No. of PD	Intra class										
	Open space								In the presence of obstacle		
	N=30		All	N=15		N=4		N=30	N=15	N=4	
	P/T	S/F		P/T	S/F	P/T	S/F				
2	98.8	97	99.1	99	98	98.2	98	97.8	94.2	97.4	
4	98.2	97.1	99.3	99	96.6	97.1	95.3	96.2	96.9	99.7	
6	98	97.3	99.3	98.4	96	95.6	91	98.3	94.6	94.6	
8	98.4	96	100	97.6	93.2	95.7	90	98.9	96.1	94.2	
10	99	97.2	99.8	97.5	93	94.9	86	99	100	99.1	
Average	98.48	96.92	99.5	98.3	95.3	96.3	92	98	96.3	97	
	Inter class										
2	100	99.8	100	100	99.5	99	98.6	99.7	99.5	100	
4	100	100	100	99.4	99.5	98.1	98	100	99	96.8	
6	99.7	100	100	99.3	99.1	96.8	96.4	99.1	97.5	95.9	
8	99.4	100	100	98	98.6	95.2	95.4	100	100	94.4	
10	99.1	99	100	97.2	97	93.9	93.9	100	96.5	92.5	
Average	99.64	99.76	100	98.7	98.7	96.6	96.4	99.7	98.5	95.9	

Table 6 Laboratory based testing of multiple PD sources

No. of sources	Determination of number of sources				Localization of sources					
	Number of tests at different positions	No. of correct identification		Accuracy (%)		Average Error (%) ±SD %				
		GMM	SOFM	GMM	SOFM	GMM	SOFM	GMM	SOFM	
2	12	12	12	100	100	0.7	0.8	0.3	0.4	
3	35	34	34	970.1	97.1	1.8	1.9	0.8	0.9	
4	24	22	23	910.6	95.8	1.4	1.5	0.9	1	
5	18	18	17	100	94.4	0.5	1.6	0.3	1.1	
6	14	12	11	850.7	78.5	2.4	3.1	1.1	1.9	
7	10	9	7	90	70	1.8	3.4	0.8	2	
8	6	6	5	100	83.3	0.6	2.3	0.2	1.5	
Average				940.9	88.4	1.3	2.1	0.6	1.2	

$$\text{Localization Error (\%)} = \frac{(E - A)}{(S1 + S2 + S3 + S4)/4} \times 100 \quad (11)$$

From the results obtained in Table 6, it can be observed that when the number of PD sources is less, both the classification techniques perform well and very close to accuracy. But when the PD number increases, the GMM performs better than the SOFM classification. Another observation can be noticed that when the number of tests with source, and sensor at different positions are taken the error in classification increases and this is somehow more for the SOFM classification technique. The overall accuracy with different tests done, is 94.9% for GMM classification, whereas this accuracy is 88.4% for SOFM classification.

4.4 Field Test Results

Field test results for three substations are summarized in Table 7, based on long-duration recordings at multiple antenna locations. As shown in Table 7, Substation 1 had three actual PD sources, but only two were detected from Position 1 of the antenna array using both techniques. This discrepancy was attributed to wall obstructions that prevented the PD signals from the transformer winding from being captured by any of the antennas.

Similar misidentification occurred with Substation 2 using only the SOFM technique. No PD sources were detected at Substation 3. To verify the PD sources and their locations, thermography tests on insulators and acoustic tests on the transformer tank using multiple ultrasonic sensors were conducted.

5 Conclusion

In this study, two unsupervised classification techniques, GMM and SOFM, were used for detecting and locating PD sources instead of supervised models, which need pre-trained data. Both techniques were tested with different PD

features obtained from the time domain signal, the corresponding frequency domain transformation PSD signal, and continuous wavelet transform signals. Frequency-domain features, or CWT scale features, extracted from a specific PD source exhibit lower variance compared to time-domain features or CWT position features. This underscores the significance of frequency-domain analysis in PD source identification.

The proposed comparison of unsupervised classification models demonstrates promising performance, making it appropriate for testing in new positions without the need for prior models. The GMM classification technique achieved accuracies of 94.9% and 90.7% in identifying the PD source numbers through laboratory and field-based testing, respectively. Whereas, for the SOFM classification technique the accuracy was 88.4% for laboratory-based testing and 87% for field-based testing. The PD source localization error is limited to around 1.4% by GMM model whereas 1.9% by SOFM model. The GMM model is more efficient in classifying and further finding the location with minimal error when a greater number of PD sources in the power system. Otherwise, both techniques are good with lesser number of sources. The technique validation methods include parametric studies, material property validation, and system-level prototype testing, all of which help confirm the model's accuracy and reliability for practical use.

This study emphasizes a method for automatic, non-contact, and unsupervised detecting and localizing individual PD sources within the power system. The implications of findings in substation maintenance and monitoring have significant practical consequences for the real-time operation of electrical power grids. These implications can span several areas, cost efficiency, including reliability, safety, and technology adoption.

As this method includes high frequency dynamic PD signal operations, a particular proposed method may not fit to every situation. So, more rigorous study is encouraged in different areas like reduction of installation cost, new

Table 7 Field testing at different substations

Name	Determination of number of sources		Different test positions						Localization of sources				
	Actual no. of sources	3	1		2		3		Error (%)	±SD %			
			GMM	SOFM	GMM	SOFM	GMM	SOFM					
Sub.-1	3	2	2	2	3	2	3	3	77.7	1.5	2.5	0.9	1.4
Sub.-2	2	2	2	2	2	2	1	1	83.3	1.4	1.4	0.5	0.5
Sub.-3	0	0	0	0	0	0	0	0	100	–	–	–	–
Average									90.7	1.45	1.9	0.7	0.9

techniques in noise reduction and cancellation, and quality signal sensing and storing system etc.

Acknowledgements This work was supported by the Korea Institute of Energy Technology Evaluation and Planning (KETEP) and the Ministry of Trade, Industry & Energy, Republic of Korea (RS-2024-00441420; RS-2024-00442817).

Data availability The data sources employed for analysis are presented in the text.

Declarations

Competing of interest The authors declare that there is no conflict of interest.

References

- König D, Rao YN (1993) Partial discharges in electrical power apparatus. VDE Verlag GmbH, Berlin and Offenbach, pp 106–108
- IEC International Standard 60270 (2000) High-voltage test techniques partial discharge measurement, international electrotechnical commission (IEC), 3rd edn. Geneva, Switzerland
- Kuffel E, Zaengl WS, Kuffel J, High voltage engineering fundamentals, 2nd edn, Newnes, Reprinted 1986. IEEE
- Sikorski W, Ziomek W, Detection, recognition and location of partial discharge sources using acoustic emission method. <https://www.intechopen.com>.
- Moore PJ, Portugues IE, Glover IA (2005) Radiometric location of partial discharge sources on energized high-voltage plant. IEEE Trans Power Delivery 20(3):2264–2272
- Tang Z, Li C, Cheng X, Wang W, Li J, Li J (2006) Partial discharge location in power transformers using wideband RF detection. IEEE Trans Dielectr Electr Insul 13(6):1193–1199
- Mishra DK, Sarkar B, Koley C, Roy NK (2017) An unsupervised Gaussian mixer model for detection and localization of partial discharge sources using RF sensors. IEEE Trans Dielectr Electr Insul 24(4):2589–2598
- Mishra DK, Dhara S, Koley C, Roy NK, Chakravorti S (2019) Self-organizing feature map based unsupervised technique for detection of partial discharge sources inside electrical substations. Measur J 147:1–11
- Markalous SM, Tenbohlen S, Feser K (2008) Detection and location of partial discharges in power transformers using acoustic and electromagnetic signals. IEEE Trans Dielectr Electr Insul 15(6):1576–1583
- Robles G, Sánchez-Fernández M, Albarraçin Sánchez R, Rojas-Moreno MV, Rajo-Iglesias E, Martínez-Tarifa JM (2013) Antenna parameterization for the detection of partial discharges. IEEE Trans Inst Meas 62(5):932–941
- Sinaga HH, Phung BT, Blackburn TR (2012) Partial discharge localization in transformers using UHF detection method. IEEE Trans Dielectr Electr Insul 19(6):1891–1900
- Ye Tian AT, Tanabe K, Miyajima K (2014) Development of locating system of pulsed electromagnetic interference source based on advanced TDOA estimation method. IEEE Trans Electr Compatibility 56(6):1326–1334
- Pinpart T, Judd MD (2010) Differentiating between partial discharge sources using envelope comparison of ultra-high-frequency signals. IET Sci Meas Technol 4(Iss. 5):256–267

14. Albarracin R, Robles G, Martinez-Tarifa JM, Ardila-Rey J (2015) Separation of sources in radiofrequency measurements of partial discharges using time–power ratio maps. *ISA Trans* 58:389–397
15. Hao L, Lewin PL, Hunter JA, Swaffield DJ, Contin A, Walton C, Michel M (2011) Discrimination of multiple PD sources using wavelet decomposition and principal component analysis. *IEEE Trans Dielect and Electr Ins* 18(5):1702–1711
16. Sinaga HH, Phung BT, Blackburn TR (2014) Recognition of single and multiple partial discharge sources in transformers based on ultra-high frequency signals. *IET Gener Transm Distrib* 8(Iss. 1):160–169
17. Boya C, Rojas-Moreno MV, Ruiz-Llata M, Robles G (2015) Location of partial discharges sources by means of blind source separation of UHF signals. *IEEE Trans Dielectr Electr Insul* 22(4):2302–2310
18. Kohonen T, “The self-organizing map”, *Proceedings of the IEEE*, Vol. 78, Iss. 9, pp. 1464–1480, 1990.
19. Luo G, Zhang D, Jet Tseng K, He J (2015) Impulsive noise reduction for transient earth voltage-based partial discharge using wavelet-entropy. *IET Sci Meas Technol* 1–8
20. Altay Ö, Kalenderli Ö (2015) Wavelet base selection for de-noising and extraction of partial discharge pulses in noisy environment. *IET Sci Meas Technol* 9(3):276–284
21. Hastie T, Tibshirani R (1996) Discriminant analysis by Gaussian mixtures. *J Royal Statistical Soc* 58:155–176
22. Abbasi AR, Gandhi CP (2022) A novel hyperbolic fuzzy entropy measure for discrimination and taxonomy of transformer winding faults. *IEEE Trans Instr and Meas* 71
23. Ansari J, Homayounzade M, Abbasi AR (2023) Load frequency control in power systems by a robust backstepping sliding mode controller design. *Energy Rep.* 10:1287–1298
24. Akbari K, Rahmani E, Abbasi A, Askari M-R (2016) Optimal placement of distributed generation in radial networks considering reliability and cost indices. *J Int Fuzzy Syst* 30:1077–1086
25. Reza Abbasi A (2022) Comparison parametric and non-parametric methods in probabilistic load flow studies for power distribution networks. *Electr Eng* 104:3943–3954

Publisher’s Note Springer Nature remains neutral with regard to jurisdictional claims in published maps and institutional affiliations.

Springer Nature or its licensor (e.g. a society or other partner) holds exclusive rights to this article under a publishing agreement with the author(s) or other rightsholder(s); author self-archiving of the accepted manuscript version of this article is solely governed by the terms of such publishing agreement and applicable law.



Dipak Kumar Mishra Dipak Kumar Mishra received the B.Tech. degree in applied electronics and instrumentation from the Biju Patnaik University of Technology, Odisha, India, in 2009, and the M.Tech. degree in instrumentation and control engineering from the National Institute of Technology, Jalandhar, India, in 2012. He has completed the Ph.D. degree from the Department of Electrical

Engineering, National Institute of Technology, Durgapur, India. He is working as assistant professor for last seven years. His research interests are signal processing, high voltage engineering, instrumentation, and control.



Ramesh Kumar Dr. Ramesh Kumar was born in Nayan Village, Rajasthan, India in 1986. He received the B.E. in Electronics Instrumentation and control engineering from the University of Rajasthan, Jaipur in 2007 and the M.Tech. And Ph.D. Degrees in Instrumentation and Control from Dr. B R Ambedkar National Institute of Technology Jalandhar, in 2009 and 2019. Since 2009-14

and 2019-present, he has been an Assistant Professor with the Electronics Department, Different Indian Collages. He is the author of two books, more than 25 in SCI/Scopus/ conferences articles. His research interests include Biomedical Instrumentation, Tomography application in medical as well as Industrial. Currently working on many applications like cube set, fuel cell technology, renewable Energy sector etc. And holds 7 patents.



Manish Kumar Singla Dr. Manish Kumar Singla is presently Assistant Professor in the Department of Interdisciplinary Courses in Engineering at Chitkara University, Rajpura, India. He did his PhD in the Electrical and Instrumentation Engineering Department at Thapar Institute of Engineering and Technology, India. He received his B.E. and M.E. degrees in Electrical Engineering from the Punjab Technical University and Thapar Institute of Engineering and Technology, in India, respectively. He has published more than 40 manuscripts in good journals and granted more than 6 patents. He is serving as an academic editor in some well-known journals. His current fields of interest include Fuel Cell, Power Systems, Artificial intelligence, Machine Learning, and Renewable Energy.

He has published more than 40 manuscripts in good journals and granted more than 6 patents. He is serving as an academic editor in some well-known journals. His current fields of interest include Fuel Cell, Power Systems, Artificial intelligence, Machine Learning, and Renewable Energy.



Mohammed H. Alsharif He is an Associate Professor in the Department of AI Convergence Electronic Engineering at Sejong University, South Korea. He received his M.Sc. Eng. and Ph.D. degrees in Electrical Engineering from the National University of Malaysia in 2012 and 2015, respectively. Dr. Alsharif’s research interests include wireless communications, network information theory, the Internet of Things (IoT), Green energy and

energy harvesting. He has authored over 160+ articles published in prestigious SCI/E journals in Electrical and Electronics/Communications Engineering, including IEEE, Elsevier, Springer, and MDPI. His work has garnered more than 7,558+ citations, with an H-index of 43+ and an I-10 index of 114+. Additionally, he has served as a guest editor for several special issues. For five consecutive years (2020–2024), Dr. Alsharif has been recognized as one of the top 2% scientists globally in Stanford University’s report.



Zong Woo Geem Prof. Zong Woo Geem works for Department of Smart City at Gachon University in South Korea. He is also a Chief Director of Smart City Research Center at the same institution. He has obtained B.Eng. from Chung-Ang University, M.Eng. and Ph.D. from Korea University, and M.Sc. from Johns Hopkins University, and researched at Virginia Tech, University of Maryland - College Park, and Johns Hopkins

University. He invented a music-inspired optimization algorithm, Harmony Search (HS), which has been applied to various scientific and engineering problems as well as social and cultural problems. His research interest includes theoretical background (e.g. novel human-experience-based derivative of HS rather than existing analytic-calculus-based derivative) and problem-specific development (e.g. problem-specific operator of HS) of phenomenon-mimicking algorithm and its applications to sustainability and culture issues.